JOURNAL OF AIRCRAFT
Vol. 29, No. 2, March–April 1992

Computational Study of Incipient Leading-Edge Separation on a Supersonic Delta Wing

S. Naomi McMillin,* James L. Pittman,† and James L. Thomas‡
NASA Langley Research Center, Hampton, Virginia 23665

A computational study on a 65 deg delta wing at a freestream Mach number of 1.60 has been conducted by obtaining conical Reynolds-averaged, Navier-Stokes solutions on a parametric series of geometries that varied in leading-edge radius and/or circular-arc camber. The computational results showed that increasing leading-edge radius or camber delay the onset of leading-edge separation on the leeside of a delta wing at a specific angle of attack. The Reynolds number was varied from 1×10^6–5×10^6 for a turbulent boundary layer and was shown to have a minor effect on the effectiveness of leading-edge radius and/or camber in delaying the onset of leading-edge separation. Both laminar and turbulent boundary-layer models were investigated at a Reynolds number of 1×10^6, and the predicted flow pattern was found to change from attached flow for the turbulent boundary-layer model to separated flow for the laminar boundary-layer model.

Nomenclature

b = span, in.
c = root chord, in.
C_p = surface-pressure coefficient
M = freestream Mach number
M_N = Mach number normal to the leading edge, $M \cos \Lambda(1 + \sin^2\alpha \tan^2\Lambda)^{1/2}$
M_x = crossflow Mach number
R = radius of curvature, in.
Re = Reynolds number
r = leading-edge radius in the crossflow plane, in.
x = longitudinal position from wing apex, in.
y = spanwise position from wing centerline, in.
z = vertical position from wing centerline, in.
α = angle of attack, deg.
α_c = angle of spanwise camber, deg.
α_N = angle of attack normal to the leading edge, deg. $\tan^{-1}(\tan\alpha/\cos\Lambda)$
Δ_s = distance from the surface of the wing to the first grid point, in.
ζ = z/(local semispan)
η = y/(local semispan)
Λ = leading-edge sweep, deg.

Introduction

THE prospect for supersonic wing design procedures based on the use of Reynolds-averaged, Navier-Stokes codes is becoming a reality with the development and experimental validation of these computational techniques. In the past, aerodynamic designs have been limited by the computational flow techniques[1–3] employed since these techniques often were only valid for a certain type of flow, i.e., separated or attached. However, the aerodynamicist prefers not to be limited to a particular type of flow so that an optimum design may make use of both attached and separated flows. One means of achieving this increased design flexibility is to employ methods that can reliably predict flow separation. The Reynolds-averaged, Navier-Stokes equations model the physical flow properties of both attached and separated flow. However, flow solvers for the equations only provide approximate solutions containing numerical approximations and truncation errors and using "models" for important physical phenomena such as turbulence.

The particular problem of interest in this study is the supersonic flow over highly swept, thin, delta wings at moderate angles of attack. The leeside flow over this type of geometry is especially interesting because of the existence of well-defined systems of vortices that significantly affect the overall aerodynamic performance of the wing. Several researchers have experimentaly investigated and classified the leeside flow over slender swept wings in supersonic flow. Stanbrook and Squire[4] originally classified separated and attached leeside flow regimes using the similarity parameters Mach number M_N and angle of attack α_N normal to the leading edge. Whitehead et al.,[5] Szodruch and Ganzer,[6] Szodruch,[7] Miller and Wood,[8] Seshadri and Narayan,[9] and Covell and Wesselmann[10] extended this work by identifying other flow regimes dependent on M_N and α_N.

In a previous effort to validate the use of a Navier-Stokes code in the supersonic wing design process,[11] a thin-layer, Navier-Stokes code[12] was used to numerically simulate the experimentally observed flow structures of Ref. 8. These flow structures included attached flow, crossflow shocks, separation bubbles, and a complex vortical system of primary and secondary vortices. The computational solutions demonstrated the capability to accurately predict the qualitative flow structures of the six flow regimes identified in Ref. 8 for sharp-edged delta wings considered in the study. However, the boundaries between the experimentally derived flow regimes, especially between attached- and separated-flow regimes, are sensitive to changes in leading-edge radius, wing thickness, and Reynolds number.[4,7,9,13] Therefore, it becomes important to determine the ability of the Navier-Stokes code to predict the effects of such parameters on the flowfield.

This article presents the results of a parametric computational study conducted to investigate the effect of leading-edge radius, leading-edge camber, Reynolds number, and

Presented as Paper 90-3029 at the AIAA 8th Applied Aerodynamics Conference, Portland, OR, Aug. 20–22, 1990; received Nov. 15, 1990; revision received March 26, 1991; accepted for publication March 26, 1991.

*Aerospace Technologist, Supersonic/Hypersonic Aerodynamics Branch, Applied Aerodynamics Division, M/S 413. Member AIAA.
†Assistant Branch Head, Aerothermal Loads Branch, Structural Mechanics Division. NASA Langley Research Center, M/S 395. Associate Fellow AIAA.
‡Branch Head, Computational Aerodynamics Branch, Fluid Mechanics Division, M/S 128. Associate Fellow AIAA.

boundary-layer model on the incipient separation of a delta wing where incipient separation is defined as the onset of leading-edge separation. The thin-layer, Navier-Stokes computational code of Ref. 12 was utilized in this computational study.

Geometry Definition

A conical 65 deg delta planform at $M = 1.6$ was chosen as the baseline geometry. This selection is based on the Mach number and angle of attack normal to the leading edge as shown in Fig. 1. As angle of attack increases, the 65 deg delta planform traverses the Stanbrook-Squire boundary that delineates attached-flow and separated-flow regimes. The effects of leading-edge radius, leading-edge camber, Reynolds number, and boundary-layer model (laminar or turbulent) on leading-edge separation would be expected to be most pronounced in the region of the Stanbrook-Squire boundary. Sensitivity of the flow pattern due to the computational boundary-layer model has been previously demonstrated.[11]

Two angles of attack were examined in this study. The $\alpha = 4$ deg point lies on the boundary and is representative of a cruise condition. The $\alpha = 8$ deg point is well into the separated-flow region and is representative of a maneuver condition.

The effect of leading-edge radius and camber on leading-edge separation is examined by varying the cross-sectional geometry. The cross-sectional shapes examined during the investigation are presented in Fig. 2. The constants were the leading-edge sweep (65 deg) and the ratio of the centerline thickness to the semispan (0.10). The effect of leading-edge radius was examined by way of three cross-sectional shapes with the following leading-edge radii: $r/(b/2) = 0.0$ (sharp), $r/(b/2) = 0.0025$ (20:1 ellipse), and $r/(b/2) = 0.01$ (blunt). The elliptic geometry was used as a baseline cross section in examining the effect of camber. A spanwise circular-arc camber was imposed on the elliptical cross-sectional geometry in the crossflow plane. The definition of the circular arc camber is as follows: $y^2 + (z + R)^2 = R^2$, where $R = (b/2)/\sin \alpha_c$. Angle of camber α_c corresponds to the spanwise camber angle at the leading edge. The following three angles of camber were examined: 4, 8, and 10 deg. At $\alpha = 4$ and 8 deg, the effects of Reynolds number ($Re = 1 \times 10^6$, 2×10^6, and 5×10^6) and boundary-layer model (laminar or turbulent) on leading-edge separation were examined.

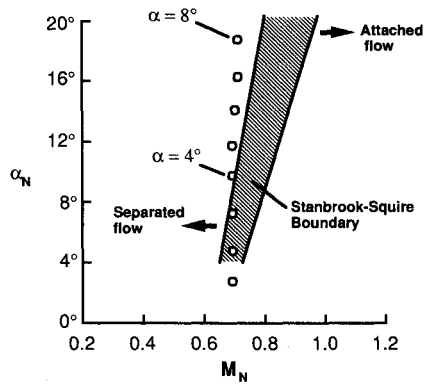

Fig. 1 Location of 65 deg delta wing at $M = 1.60$ on the α_N vs M_N chart at various angles of attack.

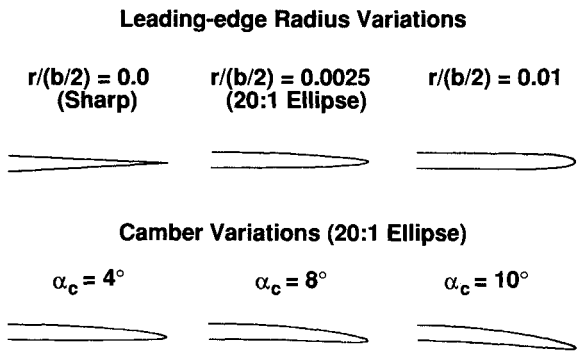

Fig. 2 Variations of the cross-sectional geometry of the 65 deg delta wing: a) $\alpha = 4$ deg; and b) $\alpha = 8$ deg.

Computational Method

The computational method utilized in the Navier-Stokes code has been discussed in detail in Refs. 12 and 14–19. The three-dimensional, time-dependent, compressible Navier-Stokes equations are transformed to a generalized coordinate system. The thin-layer approximations are then applied to the equations. The conservation form of the equations are solved with a finite-volume approach. The convective pressure terms are differenced with the upwind-biased flux-difference splitting approach of Roe,[15] whereas the shear stress and heat transfer terms are centrally differenced. The time-differencing algorithm used in the Navier-Stokes code is a spatially split approximate-factorization method.

The turbulent boundary-layer calculations are made with an isotropic, algebraic, two-layer, eddy-viscosity model developed by Baldwin and Lomax.[20] The model includes the modifications Degani and Schiff[21] incorporated to ensure that the viscous length scales are determined by the boundary layer on the body or wing in the presence of vortical flows. Newsome and Adams[22] used the model in the accurate prediction of elliptical missile body flows at large angles of attack and yaw. However, the turbulent boundary-layer model does not directly account for many effects such as compressibility, nonequilibrium, rotation, freestream turbulence, relaminarization of the boundary layer, or the location of boundary-layer transition.

The Navier-Stokes code of Ref. 12 was selected for this investigation because it had been verified previously with experimental data obtained for similar planforms and flow conditions.[11] Reference 11 documents the success of the code in predicting qualitative flow features (i.e., separation bubble, crossflow shock, vortex, separation lines, and reattachment lines) as experimentally observed in vapor-screen and oil-flow photographs and quantitative flow features such as experimental surface-pressure measurements.

The leeside surface of a flat delta wing is obviously conical and the uncambered delta wing experimental data[23] have shown the leeside flow to develop nearly conically. The computational study of Ref. 11 demonstrated that the conical Navier-Stokes solutions adequately represented the flows being investigated; thus, conical solutions were used during the present investigation. The assumption of conical flows significantly reduced the required computational resources and made it possible to examine a large number of cases.

For conical solutions, a single array of crossflow volumes is constructed such that the inflow and outflow planes are scaled by a conical transformation. At each iteration, the inflow conditions are updated with the results of the previous iteration until convergence occurs. The solutions in all cases were started impulsively from freestream initial conditions. Boundary conditions consisted of reflection conditions in the crossflow symmetry plane, no-slip and adiabatic wall temperature conditions on the body surface, and freestream conditions on the outer boundary. The bow shock and embedded shocks were captured in the grid.

For all configurations examined in this computational study, the spanwise cross-sectional geometry was nondimensionalized by the distance from the apex of the cross-sectional geometry. The conical self-similarity assumption implies that the cross-sectional geometry is extended conically forward to the apex and aft to infinity. The Reynolds number is based on the distance from the apex to the local cross-sectional geometry under consideration.

The grids used with the Navier-Stokes code were generated numerically using the code Sorenson[24] originated, which is based on the elliptic grid-generation method of Steger and Sorenson.[25] Each grid associated with a conical Navier-Stokes solution consisted of 93 radial and 121 circumferential (93 × 121) points. The grid is in the y-z plane and had a minimum spacing $\Delta s/c$ of 0.00003 at the wall, where c is the root chord of the wing. This minimum spacing was based on the criterion of having 1–2 points in the viscous sublayer. The radial grid-point stretching distribution was exponential at the body, with a smooth transition to a milder geometric stretching in the outer portion of the grid. This spacing was constructed to allow 15–20 points in the laminar boundary layer.

Computational Solutions

Shown in Table 1 are the conditions at which conical Navier-Stokes solutions were obtained in this investigation. Mach number was held constant at 1.60.

Converged solutions were usually obtained within 3500 iterations. Shown in Fig. 3 are samples of the two different types of flowfields predicted by the code throughout this investigation. The solutions presented are for the elliptic geometry at α = 4 and 8 deg with a turbulent boundary-layer model at $Re = 1 \times 10^6$. The crossflow Mach-number contour data of Fig. 3 are presented from half of the semispan to the leading edge to focus on the leading-edge flow characteristics. Note that the significant flow structures have been identified in Fig. 3. The α = 4 deg solution (Fig. 3a) has attached flow at the leading edge with a recompression occurring inboard. This recompression is sufficiently weak that it is not evident in total pressure ratio contour data (not presented here) and, thus, cannot be considered as a crossflow shock. The α = 8 deg solution (Fig. 3b) has a separated-flow pattern corresponding to a leading-edge vortex with a stronger recompression occurring atop the inboard edge of the primary vortex. Since the core of the primary vortex lies close to the surface, the vortex can be classified as a leading-edge separation bubble, as defined in Refs. 8 and 11. The code also predicts the formation of a secondary vortex beneath the primary vortex. This secondary vortex is not readily evident in the crossflow Mach-number contours of Fig. 3b, but is evident upon close examination of the velocity vectors.

Typically, attached-flow cases converged more rapidly than the separated-flow cases. The interaction of the secondary vortex and the turbulent boundary-layer model partially explains this observation. Basically, the problem is that the boundary layer and secondary vortex are merged. Thus, the basis of the turbulent length scales fluctuates between vortex properties and boundary-layer properties. The result is a fluctuation in the feeding-sheet strength and location with iteration. Because the α = 8 deg solution has converged to 2.5 orders of magnitude in residual and the unsteadiness in surface pressure distribution (not presented here) is confined to the secondary vortex/boundary-layer interaction region, the solution was considered to be acceptable.

Another convergence problem that arose concerned vortical flow solutions obtained using the laminar boundary-layer model. For such solutions, the size and location of the primary vortex was unable to converge. This corresponded to an order of magnitude reduction of less than two in residual and an unsteadiness in the surface pressure distribution from the edge of the vortex to the leading edge (not presented here).

In the code, the time step is allowed to vary locally from cell to cell based on the Courant number and the cell conditions. In an effort to correct the above convergence problem, the time-step routine was modified to hold the time step constant for the first 20% of the cells away from the surface, corresponding essentially to the boundary-layer region. Thus, the time step used through this region was the time step associated with the edge of the region and the modification increased the Courant number of the small cells close to the surface. This modification resulted in a dramatic improvement in the convergence of the laminar boundary-layer solutions. All laminar boundary-layer solutions that were obtained using the modified time-step routine are denoted in Table 1. No improvement in convergence history was noted when the modified time-step routine was used for the turbulent boundary-layer solutions with separated flow at the leading edge, such as that shown in Fig. 3b. This observation supports the hypothesis that the convergence problem with the turbulent boundary-layer solutions is related to the interaction of the secondary vortex and turbulent boundary-layer model.

Table 1 Conditions of computational solutions obtained

Cross-sectional geometry	Reynolds number		
	1×10^6	2×10^6	5×10^6
$r/(b/2)$ = 0.0, α_c = 0 deg	T,L[a,b]	T,L[a]	T,L[a]
$r/(b/2)$ = 0.0025, α_c = 0 deg	T,L[a]	T	T
$r/(b/2)$ = 0.0, α_c = 0 deg	T,L	T	T
$r/(b/2)$ = 0.0025, α_c = 4 deg	T,L[a]	T	T
$r/(b/2)$ = 0.0025, α_c = 8 deg	T,L[a]	T	T
$r/(b/2)$ = 0.0025, α_c = 10 deg	T,L[a]	T	T

L—Laminar boundary-layer model.
T—Turbulent boundary-layer model.
[a]Time-step constant through boundary layer for α = 4 deg.
[b]Time-step constant through boundary layer for α = 8 deg.

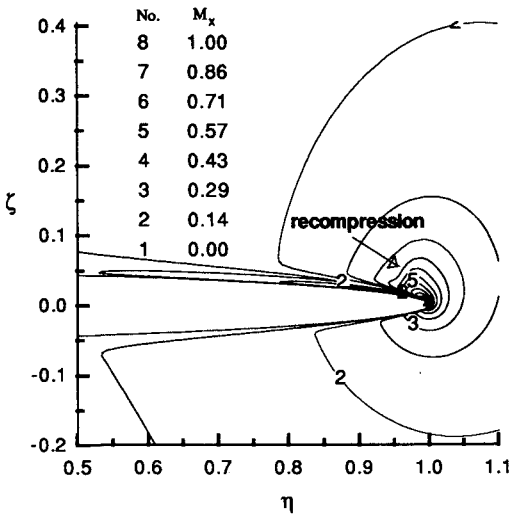

a) Crossflow Mach number contours

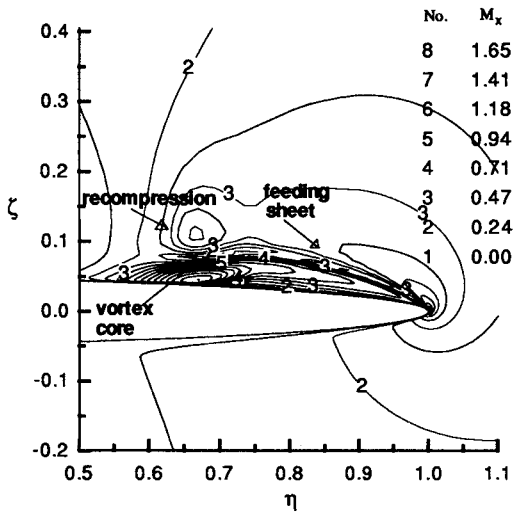

b) Surface-pressure coefficient distributions

Fig. 3 Crossflow Mach number contour data from the turbulent boundary-layer solutions for the elliptical cross-sectional geometry at α = 4 and 8 deg, M = 1.60, and $Re = 1 \times 10^6$.

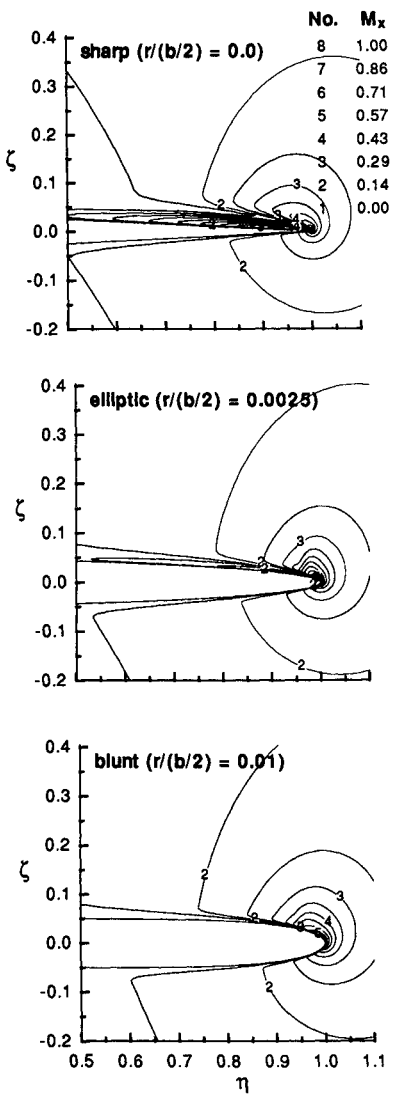

a) Crossflow Mach number contours

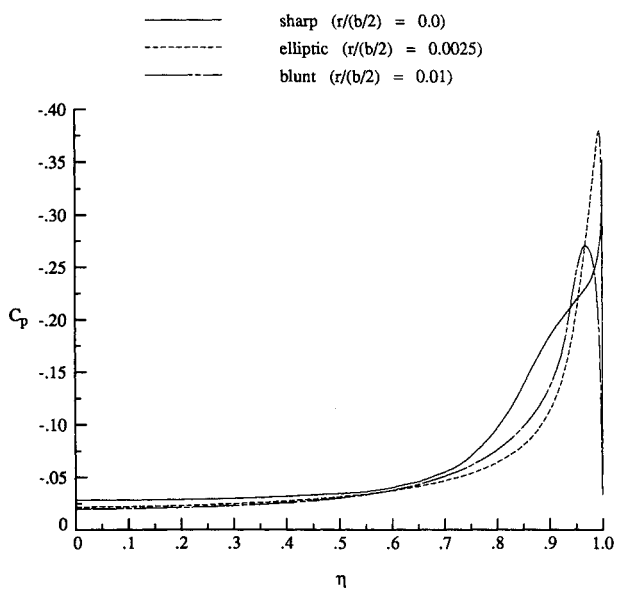

b) Surface-pressure coefficient distributions

Fig. 4 The effect of leading-edge radius on the turbulent boundary-layer solutions at α = 4 deg, M = 1.60, and Re = 1 × 10^6.

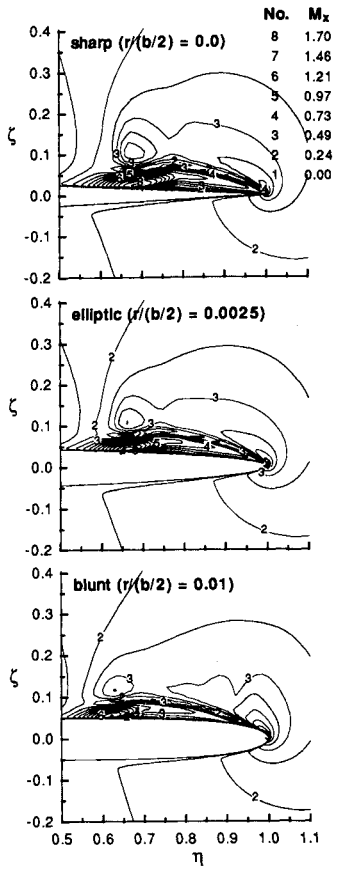

a) Crossflow Mach number contours

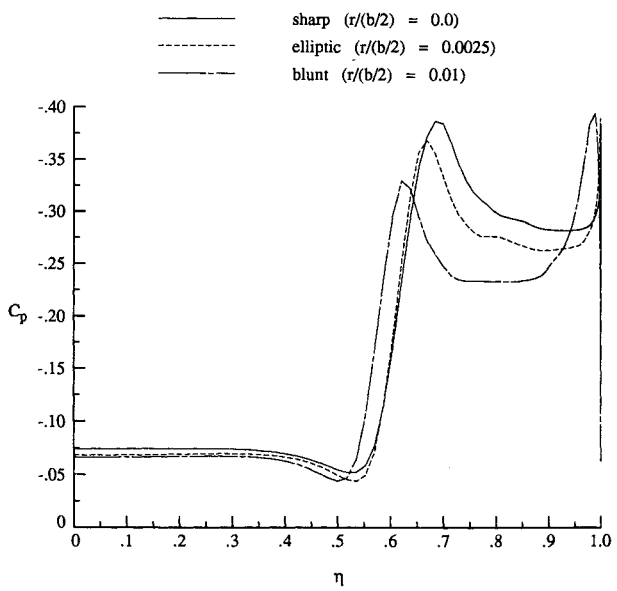

b) Surface-pressure coefficient distributions

Fig. 5 The effect of leading-edge radius on the turbulent boundary-layer solutions at α = 8 deg, M = 1.60, and Re = 1 × 10^6.

Results and Discussion

The effects of geometry and flow conditions on the flow separation characteristics of a 65 deg delta wing at M = 1.60 are discussed here. The data is presented in the form of cross-flow Mach-number contours and surface-pressure coefficient distributions.

Leading-Edge Radius and Camber Effects

Presented in Fig. 4 are the data from the turbulent boundary-layer solutions for a variation in leading-edge radius

at $\alpha = 4$ deg and $Re = 1 \times 10^6$. The crossflow Mach-number data for the sharp leading-edge [$r/(b/2) = 0.0$] solution form a series of closed elongated contours just above the upper surface that indicate a separation bubble forming at the leading edge. This bubble is weak as determined by the diffused core; however, upon close examination of the crossflow velocity vectors (not presented here) a separation at the leading edge clearly exists to form a recirculation region in the flow. The elliptic [$r/(b/2) = 0.0025$] and blunt [$r/(b/2) = 0.01$] data illustrate that by imposing a leading-edge radius on the cross-sectional geometry the flow remains attached at the leading edge. The crossflow Mach-number data of these rounded leading-edge solutions show a recompression occurring just inboard of the leading edge. The separated- and attached-flow patterns yield different surface-pressure coefficient distributions with the attached-flow cases yielding a much smoother distribution out to the leading edge as seen in Fig. 4b. The inflections in the surface-pressure coefficient distribution of the sharp leading-edge solution correspond to the recirculation region in the predicted leading-edge separation bubble.

The effect of leading-edge radius at the higher angle of attack of 8 deg is presented in Fig. 5. The contour data of Fig. 5a for the sharp leading-edge geometry show that by increasing the angle of attack the separation at the leading edge forms a well-defined feeding sheet and core with a recompression occurring atop the inboard edge of the primary vortex. The elliptic and blunt solutions also predicted a primary vortex separating at the leading edge. Thus, the effectiveness of leading-edge radius in preventing leading-edge separation lessens as angle of attack increases.

However, the data of Fig. 5 show that leading-edge radius still influences the primary vortex field at the higher angle of attack. The contour data of Fig. 5a show that with an increase in leading-edge radius the primary vortex becomes slightly elongated such that the inboard edge of the vortex moves slightly inboard. This observation is more readily evident in the surface-pressure coefficient distributions of Fig. 5b where the sharp decrease in surface-pressure coefficient indicates the inboard edge of the primary vortex moves inboard with an increase in leading-edge radius. The well-defined pressure coefficient minimum between $\eta = 0.50$ and $\eta = 0.70$ diminishes with an increase in leading-edge radius. This corresponds to a decrease in the maximum crossflow Mach number of the vortex core with increasing leading-edge radius as is evident in Fig. 5a. Also shown in Fig. 5a is a decrease in the strength of the recompression atop the primary vortex with increasing leading-edge radius. Thus, at the higher angle of attack the effect of leading-edge radius is to weaken the primary vortex and recompression.

The elliptical cross-sectional geometry was used as the baseline geometry for examining the effects of spanwise circular-arc camber. The turbulent boundary-layer solutions for the $\alpha_c = 4$, 8, and 10 deg geometries at $\alpha = 8$ deg and $Re = 1 \times 10^6$ are presented in Fig. 6. The corresponding solution for the uncambered elliptical cross-sectional geometry is presented in Fig. 5a. The crossflow Mach-number data of Figs. 5a and 6a show that as the camber angle is increased from 0 to 4 deg the primary vortex predicted for the uncambered elliptical cross-sectional shape weakens; that is the crossflow Mach number of the vortex core lessens and the surface-pressure coefficient minimum decreases. At $\alpha_c = 8$ deg, the primary vortex is even weaker as is evident by the diffused core. However, the crossflow velocity vectors for this case (not presented here) clearly show a recirculation region beginning at the leading edge. The inflections in the surface-pressure coefficient distribution for the $\alpha_c = 8$ deg case correspond to this recirculation region. Finally at $\alpha_c = 10$ deg, the flow is attached at the leading edge with a recompression occurring inboard. Thus, the effect of increasing the spanwise circular-arc camber is to weaken and eventually eliminate leading-edge separation.

Reynolds Number Effects

Turbulent boundary-layer solutions were obtained for each geometry at $Re = 1 \times 10^6$, 2×10^6, and 5×10^6. A comparison of these solutions shows that a variation in Reynolds-number (in this range of 1×10^6–5×10^6) did not significantly alter the effectiveness of leading-edge radius and camber in delaying the onset of leading-edge separation. However, a variation of Reynolds number affects the strength of the primary and secondary flow structures.

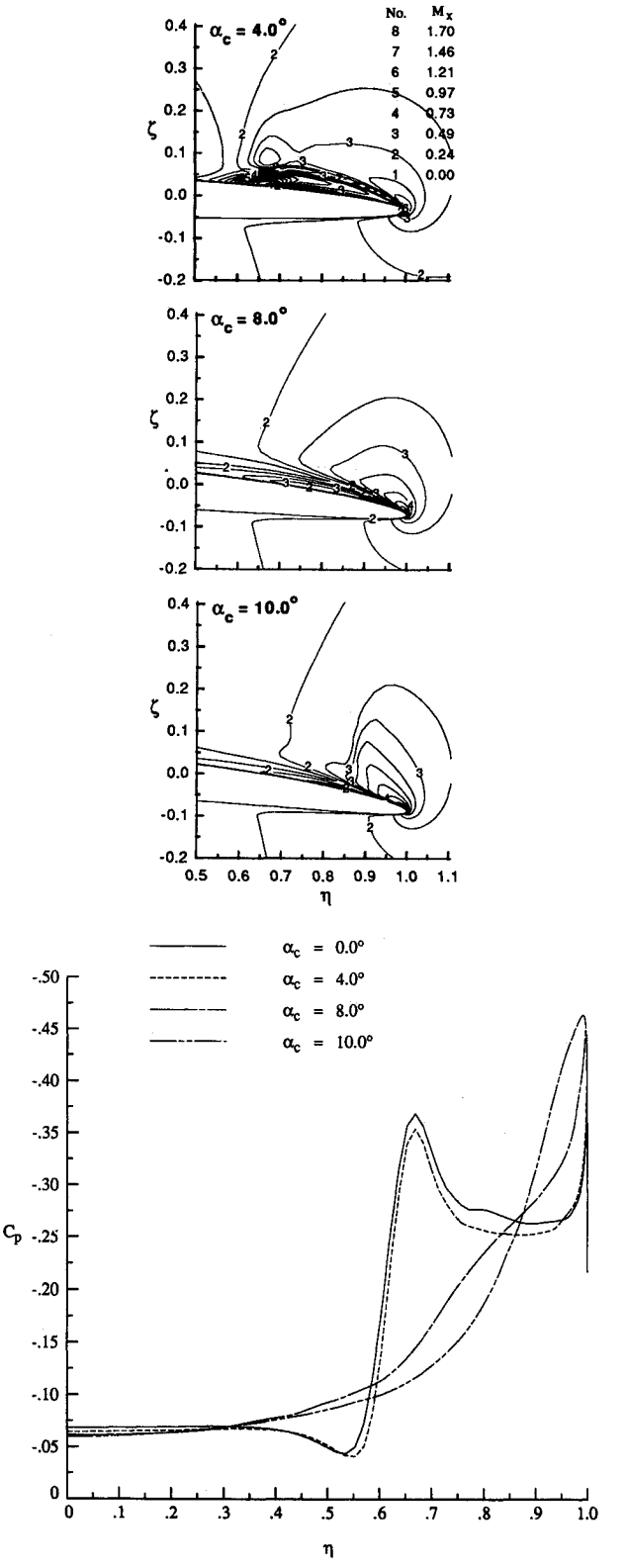

Fig. 6 The effect of camber on the turbulent boundary-layer solutions at $\alpha = 8$ deg, $M = 1.60$, and $Re = 1 \times 10^6$.

Presented in Fig. 7 is the typical effect of Reynolds number for a fully turbulent boundary layer for a separated-flow case. The separated-flow case is the uncambered elliptical cross-sectional geometry at $\alpha = 8$ deg. The flow pattern predicted for this geometry at $\alpha = 8$ deg is evident in Fig. 5a (for $Re = 1 \times 10^6$) and is that of a primary vortex separating at the leading edge with a recompression atop the primary vortex. Figure 7 presents the surface-pressure coefficient distributions from the turbulent boundary-layer solutions for this case at Reynolds numbers of 1×10^6, 2×10^6, and 5×10^6. These data and the crossflow Mach-number contour data (not presented here) show that Reynolds number did not affect the prediction of separated flow for this case. An increase in Reynolds number increases the well-defined pressure minimum that occurs between $\eta = 0.60$ and $\eta = 0.70$. This increase corresponds to an increase in the crossflow Mach number of the vortex core with an increase in Reynolds number. The crossflow Mach number and surface-pressure coefficient

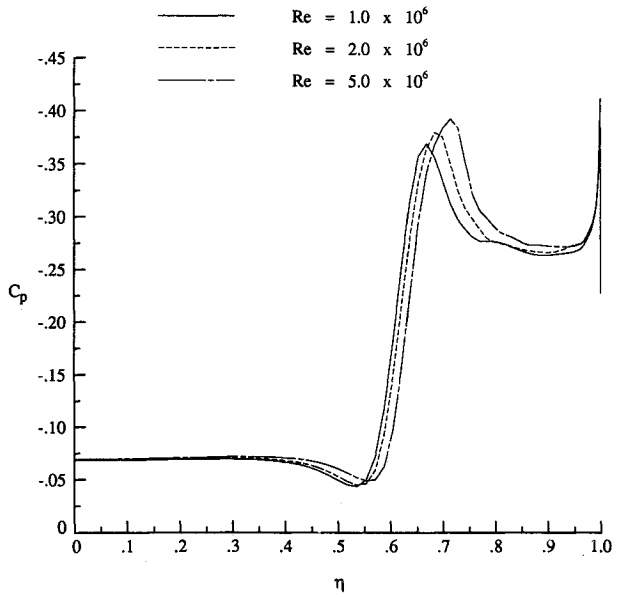

Fig. 7 The effect of Reynolds number on the turbulent boundary-layer solution for the elliptical cross-sectional geometry at $\alpha = 8$ deg, $M = 1.60$, and $Re = 1 \times 10^6$.

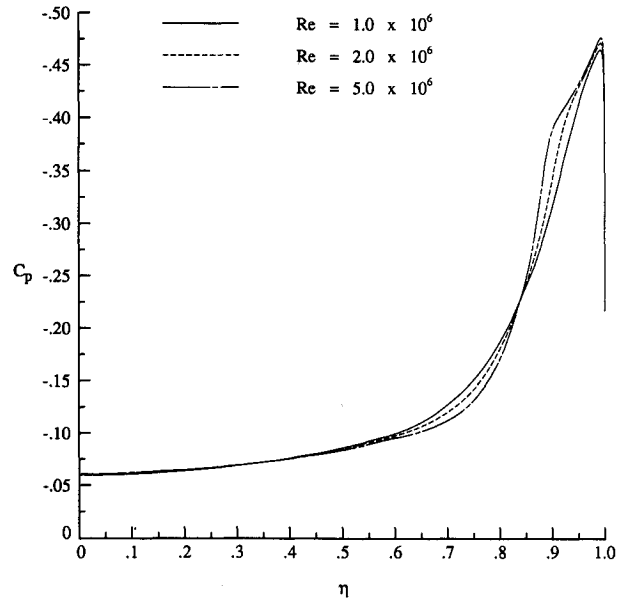

Fig. 8 The effect of Reynolds number on the turbulent boundary-layer solution for the 10-deg cambered geometry at $\alpha = 8$ deg, $M = 1.60$, and $Re = 1 \times 10^6$: a) crossflow Mach number contours; and b) surface-pressure coefficient distributions.

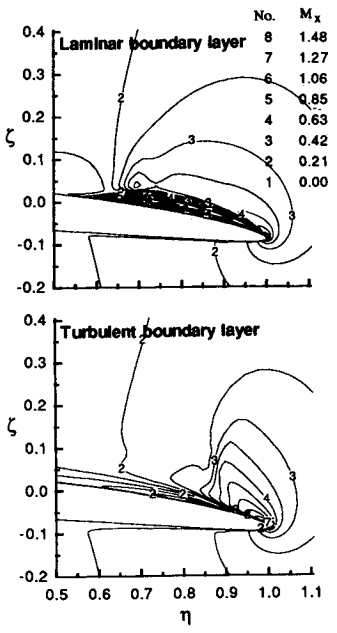

a) Crossflow Mach number contours

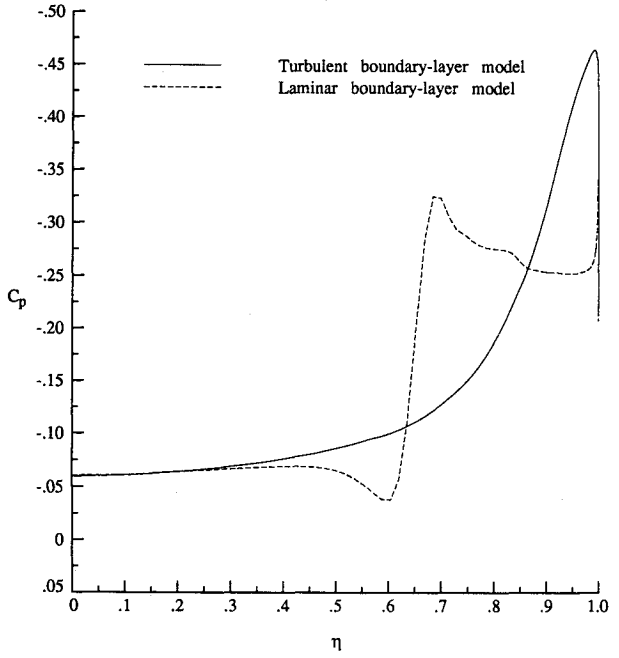

b) Surface-pressure coefficient distributions

Fig. 9 The effect of boundary-layer model on the prediction of flow for the 10-deg cambered geometry at $\alpha = 8$ deg, $M = 1.60$, and $Re = 1 \times 10^6$.

data also show that the vortex core moves slightly outboard with increasing Reynolds number. Thus, the predicted primary vortex becomes stronger and more compact with an increase in Reynolds number.

Presented in Fig. 8 is the effect of Reynolds number for an attached-flow case. The attached-flow case is the $\alpha_c = 10$ deg geometry at $\alpha = 8$ deg. The flow pattern predicted for this geometry is evident in Fig. 6a and is that of attached flow at the leading edge with a recompression occurring slightly inboard. Figure 8 presents the surface-pressure coefficient distributions from the turbulent boundary-layer solutions for this case at Reynolds numbers of 1×10^6, 2×10^6, and 5×10^6. For all Reynolds numbers, the flow remains attached at the leading edge. However, the inflections in the surface-pressure coefficient distributions in the region of the crossflow shock indicate that separation at the base of the recompression occurs as Reynolds number increases. This separation is very

weak and is evident only upon close examination of the velocity vectors.

Boundary-Layer Effects

The sensitivity of predicted flow pattern due to boundary-layer model has been documented in Ref. 11. This sensitivity is limited to the region on the M_N and α_N chart where the flow transitions from separated flow at the leading edge to attached flow at the leading edge (i.e., near the Stanbrook-Squire boundary). The transitional flow pattern was identified in Ref. 11 as the leading-edge separation bubble with shock flow pattern. As discussed previously, the 65 deg delta wing of this investigation at $M = 1.60$ and $\alpha = 0$ to 8 deg falls within this transition region (Fig. 1).

Laminar boundary-layer solutions were obtained for each geometry at $Re = 1 \times 10^6$. These solutions were compared with their corresponding turbulent boundary-layer solutions. For those turbulent boundary-layer solutions that predicted separated flow at the leading edge, the effect of boundary-layer model was limited to the strength of the secondary vortex as documented in Ref. 11.

However, a significant effect of boundary-layer model was observed for those cases where the turbulent boundary-layer solutions predicted attached flow at the leading edge. Presented in Fig. 9 is the effect of boundary-layer model on the $\alpha_c = 10$ deg geometry at $\alpha = 8$ deg and $Re = 1 \times 10^6$. The contour data of Fig. 9a show that the turbulent solution predicts an attached flow at the leading edge with a recompression occurring slightly inboard of the leading edge. However, the laminar boundary-layer solution predicts a primary vortex separating at the leading edge with a crossflow shock occurring atop the vortex. These different flow patterns yield different surface-pressure coefficient distributions as evident in Fig. 9b. The same trend with boundary-layer model was found to be true of all cases that yielded attached-flow patterns with the use of the turbulent boundary-layer model.

Concluding Remarks

A computational study has been conducted to investigate the effect of leading-edge radius and camber on the incipient separation of a 65 deg delta wing at $M = 1.60$. The study was conducted by obtaining conical, turbulent boundary-layer Navier-Stokes solutions on a parametric series of geometries that varied in leading-radius and/or spanwise circular-arc camber. Solutions were obtained at 4- and 8-deg angle of attack at Reynolds numbers (based on root chord) or 1×10^6, 2×10^6, and 5×10^6. At 4-deg angle of attack, increasing the leading-edge radius allowed the flow to remain attached at the leading edge. At 8-deg angle of attack, the effectiveness of leading-edge radius in delaying leading-edge separation decreased. However, increasing the angle of spanwise circular-arc camber allowed the flow to remain attached at the leading edge for a moderately rounded leading edge.

Reynolds number was varied from 1×10^6–5×10^6 for the turbulent boundary-layer model during this investigation. In this range of Reynolds number, no influence of Reynolds number was observed on the effectiveness of leading-edge radius and camber to delay leading-edge separation although the strength of the primary and secondary flow structures was affected. For separated flow at the leading edge, the primary vortex became slightly stronger and more compact with increasing Reynolds number. For attached flow at the leading edge, a weak separation at the base of the crossflow shock occurs as Reynolds number increases.

The effect of boundary-layer model (laminar vs turbulent) was investigated at $Re = 1 \times 10^6$. For cases that yielded attached flow for the turbulent boundary layer, separated flow was predicted for the laminar boundary layer. For those cases that yielded separated flow with the use of the turbulent boundary-layer model, the laminar boundary-layer model also predicted separated flow.

References

[1]Brown, C., McLean, F., and Klunker, E., "Theoretical and Experimental Studies of Cambered and Twisted Wings Optimized for Flight at Supersonic Speeds," *Proceedings of the 2nd International Congress of Aeronautical Sciences, Advances in Aeronautical Science*, Vol. 3, edited by T. Von Karman et al., Pergamon, Oxford, 1962, pp. 415–431.

[2]Pittman, J. L., Miller, D. S., and Mason, W. H., "Supersonic, Nonlinear, Attached-Flow Wing Design for High Lift with Experimental Validation," NASA TP-2336, Aug. 1984.

[3]Lan, C. E., and Chang, J. F., "VORCAM—A Computer Program for Calculating Vortex Lift Effect of Cambered Wings by the Suction Analogy," NASA CR-165800, Nov. 1981.

[4]Stanbrook, A., and Squire, L. C., "Possible Types of Flow at Swept Leading Edges," *Aeronautical Quarterly*, Vol. XV, Feb. 1964, pp. 72–82.

[5]Whitehead, A. H., Hefner, J. N., and Rao, D. M., "Lee-Surface Vortex Effects Over Configurations in Hypersonic Flow," AIAA Paper 72-77, San Francisco, CA, Jan. 1972.

[6]Szodruch, J., and Ganzer, U., "On the Lee-Side Flow Over Delta Wings at High Angle of Attack," AGARD 247, Sept. 1978.

[7]Szodruch, J., "Lee-Side Flow for Slender Delta Wings of Finite Thickness," NASA TM-75753, March 1980.

[8]Miller, D. S., and Wood, R. M., "Lee-Side Flow Over Delta Wings at Supersonic Speeds," NASA TP-2430, June 1985.

[9]Seshadri, S. N., and Narayan, K. Y., "Lee-Surface Flow Over Delta Wings at Supersonic Speeds," NAL TM AE 8610, Bangalore, India, Sept. 1986.

[10]Covell, P., and Wesselmann, G., "Flow-Field Characteristics and Normal-Force Correlations for Delta Wings from Mach 2.4 to 4.6," AIAA Paper 89-26, Reno, NV, Jan. 1989.

[11]McMillin, S. N., Thomas, J. L., and Murman, E. M., "Navier-Stokes and Euler Solutions for Lee-Side Flows Over Supersonic Delta Wings—A Correlaiton with Experiment," NASA TP-3035, Dec. 1990.

[12]Thomas, J. L., and Newsome, R. W., "Navier-Stokes Computations of Lee-Side Flow Over Delta Wings," *AIAA Journal*, Vol. 27, Dec. 1989, pp. 1673–1679.

[13]Szodruch, J., and Peake, D. J., "Leeward Flow Over Delta Wings at Supersonic Speeds," NASA TM-81187, April 1980.

[14]Vatsa, V. N., Thomas, J. L., and Wedan, B., "Navier-Stokes Computations of a Prolate Spheroid at Angle of Attack," *Journal of Aircraft*, Vol. 26, Nov. 1989, pp. 986–993.

[15]Roe, P. L., "Characteristics Based Schemes for the Euler Equations," *Annual Review of Fluid Mechanics*, Vol. 18, Palo Alto, California, 1986, pp. 337–365.

[16]Anderson, W. K., Thomas, J. L., and Van Leer, B., "Comparison of Finite Volume Flux Splitting Methods for the Euler Equations," *AIAA Journal*, Vol. 24, Sept. 1986, pp. 1453–1460.

[17]Van Leer, B., Thomas, J. L., Roe, P. L., and Newsome, R. W., "A Comparison of Numerical Flux Formulas for the Euler and Navier-Stokes Equations," AIAA Paper 87-1104, Honolulu, HI, June 1987.

[18]Thomas, J. L., Taylor, S. K., and Anderson, W. K., "Navier-Stokes Computations of Vortical Flow Over Low Aspect Ratio Wings," *AIAA Journal*, Vol. 28, Feb. 1990, pp. 205–212.

[19]Krist, S. K., Thomas, J. L., Sellers, W. L., III, and Kjelgaard, S. O., "An Embedded Grid Formulation Applied to a Delta Wing," AIAA Paper 90-0429, Reno, NV, Jan. 1990.

[20]Baldwin, B. S., and Lomax, H., "Thin-Layer Approximation and Algebraic Model for Separated Turbulent Flows," AIAA Paper 78-257, Huntsville, AL, Jan. 1978.

[21]Degani, C., and Schiff, L. B., "Computations of Supersonic Viscous Flows Around Pointed Bodies at Large Incidence," AIAA Paper 83-0034, Reno, NV, Jan. 1983.

[22]Newsome, R. W., and Adams, M. S., "Numerical Simulations of Vortical Flow Over an Elliptical-Body Missile at High Angles of Attack," AIAA Paper 86-0559, Reno, NV, Jan. 1986.

[23]Wood, R. M., and Watson, C. B., "Study of Lee-Side Flows Over Conically Cambered Delta Wings at Supersonic Speeds," NASA TP 2660, July 1987.

[24]Sorenson, R. L., "A Computer Program to Generate Two-Dimensional Grids About Airfoils and Other Shapes by the Use of Poisson's Equation," NASA TM-82298, May 1980.

[25]Steger, J. L., and Sorenson, R. L., "Automatic Mesh Point Clustering Near Boundary in Grid Generation with Elliptic Partial Differential Equations," *Journal of Computational Physics*, Vol. 33, Dec. 1979, pp. 405–410.